

Pulse Phase-coherent Timing and Spectroscopy of CXOU J164710.2–45521 Outbursts

Guillermo A. Rodríguez Castillo,^{1,2} Gian Luca Israel,² Paolo Esposito,³ José A. Pons,⁴ Nanda Rea,^{5,6} Roberto Turolla,^{7,8} Daniele Viganò,^{4,5} and Silvia Zane⁸

¹Dipartimento di Fisica, Sapienza Università di Roma, Piazzale Aldo Moro 5, 00185, Rome, Italy

²INAF-Astronomical Observatory of Rome, via Frascati 33, 00040, Monte Porzio Catone, Italy

³INAF-IASF Milano, Via E. Bassini 15, I-20133 Milano, Italy

⁴Departament de Física Aplicada, Universitat d'Alacant, Ap. Correus 99, 03080, Alacant, Spain

⁵Institute of Space Sciences (CSIC-IEEC), Campus UAB, Faculty of Science, Torre CS-parell, E-08193 Barcelona, Spain

⁶Astronomical Institute “Anton Pannekoek”, University of Amsterdam, Postbus 94249, 1090 GE Amsterdam, The Netherlands

⁷Department of Physics, University of Padova, Via Marzolo 8, 35131, Padova, Italy

⁸Mullard Space Science Laboratory, University College London, Holmbury St. Mary, Dorking, Surrey, RH5 6NT, UK

MNRAS, published online May 8, 2014. doi: 10.1093/mnras/stu603

ABSTRACT

We present a long-term phase-coherent timing analysis and pulse-phase resolved spectroscopy for the two outbursts observed from the transient anomalous X-ray pulsar CXOU J164710.2–455216. For the first outburst we used 11 *Chandra* and *XMM-Newton* observations between September 2006 to August 2009, the longest baseline yet for this source. We obtain a coherent timing solution with $P = 10.61065583(4)$ s, $\dot{P} = 9.72(1) \times 10^{-13}$ s s⁻¹ and $\ddot{P} = -1.05(5) \times 10^{-20}$ s s⁻². Under the standard assumptions this implies a surface dipolar magnetic field of $\sim 10^{14}$ G, confirming this source as a standard *B* magnetar. We also study the evolution of the pulse profile (shape, intensity and pulsed fraction) as a function of time and energy. Using the phase-coherent timing solution we perform a phase-resolved spectroscopy analysis, following the spectral evolution of pulse-phase features, which hints at the physical processes taking place on the star. The results are discussed from the perspective of magneto-thermal evolution models and the untwisting magnetosphere model. Finally, we present similar analysis for the second, less intense, 2011 outburst. For the timing analysis we used *Swift* data together with 2 *XMM-Newton* and *Chandra* pointings. The results inferred for both outbursts are compared and briefly discussed in a more general framework.

Key words: stars: neutron – stars: magnetars – star: individual (CXOU J164710.2-455216) – X-rays: bursts

1 INTRODUCTION

Soft γ -repeaters (SGRs) and anomalous X-ray pulsars (AXPs) are isolated neutron stars (INSs) with prominent high-energy manifestations. They are characterized by rotational periods in the 0.3–12 s range and period derivatives (usually) larger than those typical of the radio-pulsar population ($\dot{P} \sim 10^{-13} - 10^{-10}$ s/s). They exhibit peculiar flaring activity (see e.g. Mereghetti 2013) over a large range of time-scales (milliseconds to minutes) and luminosities ($L \sim 10^{38-47}$ erg s⁻¹). Estimates of their magnetic field, derived under the usual assumptions for isolated rotation-powered pulsars, place them at the high end of the pulsar population ($B \approx 10^{14-15}$ G). This, and other direct (Tiengo et al. 2013) and indirect evidences, suggests that they host an ultramagnetized neutron star, or magnetar (Duncan & Thompson 1992, Thompson & Duncan 1995).

Since the detection of SGRs/AXPs as persistent X-ray

sources, one of the main concern has been the imbalance between the emitted luminosity and the rotational energy loss rate, \dot{E} . Rotation is believed to be the standard mechanism that provides the energy output in canonical radio-pulsars. However, in SGRs/AXPs \dot{E} is orders of magnitude below L_X , although in some transient sources the rotational energy loss rate may exceed luminosity in the quiescent state (see e.g. Rea et al. 2012a). Energy might be supplied by accretion, if a feeding companion is present as is the case of many X-ray (binary) pulsars. Despite intensive searches, however, no binary companions have been detected so far around SGRs/AXPs (see e.g. Woods et al. 2000; Camilo et al. 2006 for the tightest constraints).

A more likely alternative is that SGRs/AXPs are magnetically powered sources in which the decay/rearrangement of their (huge) magnetic field is responsible for both their persistent and bursting emission. Nowadays the magnetar model appears to be the more viable one and it will be assumed in this investiga-

tion, in particular for what concerns the timing and spectral analysis. In the following we shall refer to SGRs/AXPs as the “magnetar candidates”, or simply as magnetars. Alternative scenarios have been proposed with varying degree of success to explain the SGRs/AXPs phenomenology, and include fallback discs (see e.g. Alpar et al. 2012), Thorne-Żytkow objects (van Paradijs, Taam, & van den Heuvel 1995), strange/quark/hybrid stars (see e.g. Horvath 2005; Xu 2007; Ouyed, Leahy & Niebergal 2010) and fast rotating, highly-magnetized ($B \sim 10^{8-9}$ G) massive white dwarfs (Paczynski 1990; Malheiro, Rueda & Ruffini 2012), among others (see Turolla & Esposito 2013, section 5 and Mereghetti 2008, section 7 for overviews).

1.1 OUTBURSTS IN MAGNETARS

Most of the known magnetar candidates are transient sources. A transient episode in a magnetar can be defined as an outburst characterized by a rapid (minutes–hours) increase of the persistent flux by a factor of ~ 10 –1000, with a subsequent decay back to the quiescent level on time-scales of months–years. Short bursts, which usually trigger detection, are emitted in the early phases of the outburst. Recurrent outbursts have been observed in a few sources (see Rea & Esposito, 2011 for a review).

Within the magnetar picture, outbursts occur quite naturally. According to our current understanding, one of the major differences between the magnetar candidates and pulsars is not (or not only) the higher value of the dipole field (there are low-field magnetars with $B \lesssim 10^{13}$ G and high-field pulsars with $B \gtrsim 10^{13}$ G), but the presence of a strong toroidal component in the internal field (Turolla et al. 2011 and references therein). It is the dissipation of the internal field which powers the magnetar bursting/outbursting behaviour by injecting energy deep in the star crust and/or by inducing displacements of the surface layers, with the consequent “twisting” of the external field (e.g. Thompson, Lyutikov & Kulkarni 2002; Perna & Pons 2011; Pons & Rea 2012). The rate at which these episodes occur is different in different sources and is believed to depend mostly on the star magnetic field at birth and on its age.

Since the discovery the first confirmed transient magnetar in 2003 (XTE J1810-197, which exhibited a flux enhancement by a factor of > 100 ; Ibrahim et al. 2004), outbursts have been the object of much interest. This stems from the possibility of testing, during the outburst decay, theoretical predictions over a relatively large luminosity range in a single source, where a large number of important parameters are not changing, like, e.g., distance, mass, radius, age, viewing geometry (see e.g. Bernardini et al. 2009; Albano et al. 2010; Rea et al. 2013). CXOU J164710.2–455216 is among the transients with the larger flux variation. Following the outburst of 2006 September, in fact, its flux grew by a factor of $\gtrsim 300$ (Campana & Israel 2006).

1.2 CXOU J164710.2-455216

The source, CXOU J1647-45 for short, was discovered by Muno et al. (2006) using *Chandra* observations, with a period of 10.6107(1) s. An important feature of CXOU J1647-45 is that it very likely belongs to the young, massive Galactic starburst cluster Westerlund 1. This provides hints about its progenitor and also about its distance. Indeed, studies of the massive stellar population of Westerlund 1 indicate a distance of ~ 5.0 kpc and a progenitor with an initial mass $M_i > 40 M_\odot$ (Crowther et al. 2006; Muno et al. 2006; Negueruela Clark & Ritchie 2010).

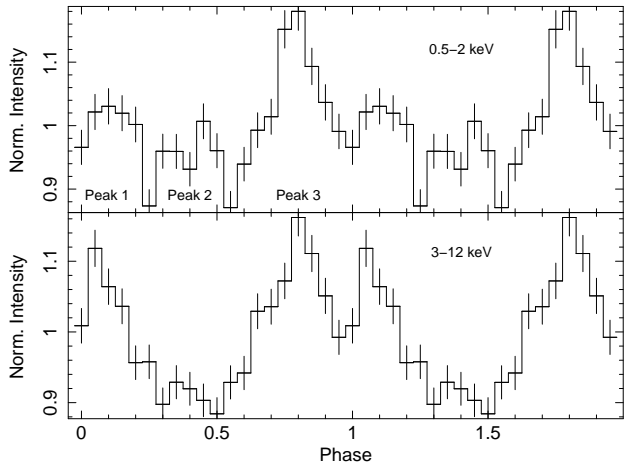


Figure 1. Upper panel: pulse profile of CXOU J164710.2–455216, observation 060922 at the 0.5 – 2.0 keV energy range. Lower panel: The same observation at the 3.0 – 12.0 keV energy range. Note that the peak at phase ~ 0.4 is missing at higher energies.

Another prominent feature of CXOU J1647-45, as mentioned before, is that it underwent an outburst with one of the largest flux enhancements observed up to now among the magnetars. On September 2006 the Burst Alert Telescope (BAT) on board the *Swift* satellite detected an intense burst in the direction of the Westerlund 1. A second observation, performed 13 h later by *Swift*, with its narrow field instrument, the X-ray telescope (XRT), found CXOU J1647-45 brighter by a factor of ~ 300 . Between February 2007 and August 2009 we requested and obtained five *XMM-Newton* pointings which, together with the September 2006 post-outburst observations, were aimed at studying the evolution of the timing and spectral properties of CXOU J1647-45 over a range covering a factor of about 50 in flux, from $\sim 10^{35}$ erg/s down to near the quiescent level, at a few 10^{33} erg/s (Campana & Israel 2006). Deep observational campaign in the radio, near-infrared and hard X-ray bands did not detect any convincing counterpart (Muno et al. 2006; Israel et al. 2007), in contrast with the results obtained for other transient magnetars, e.g. XTE J1810 (Israel et al. 2004; Camilo et al. 2006) and 1E 1547 (Camilo et al. 2007; Israel et al. 2009).

On 2011 September 19 *Swift*-BAT recorded four relatively bright bursts from a position consistent with that of CXOU J1647-45 (Baumgartner et al. 2011), approximately five years after the 2006 outburst onset. A subsequent *Swift*-XRT pointing found CXOU J1647-45 at a flux level of $\sim 7.8 \times 10^{-11}$ erg cm $^{-2}$ s $^{-1}$, more than 200 times higher than its quiescent level (2.7×10^{-13} erg cm $^{-2}$ s $^{-1}$, Muno et al. 2007), and more than 100 times brighter than the latest *XMM-Newton* pointing of August 2009 (Israel, Esposito & Rea 2011): the pulsar entered a new outburst phase.

Several *Swift* observations were requested together with two director’s discretionary time observations, one with *XMM-Newton* and one with *Chandra*. The latter two were carried out 9 and 34 days after the BAT trigger, respectively. A further *XMM-Newton* pointing scheduled for April 2012 was cancelled because of a strong solar storm. The *XMM-Newton* and *Chandra* pointings aimed at comparing the properties of the 2006 and 2011 outbursts.

CXOU J1647-45 2006 outburst has been analyzed in previous investigations. In particular timing and spectral analyses have been performed by Israel et al. (2007) and Woods et al. (2011; both phase-coherent), and An et al. (2013; period evolution). Their timing results are summarized in Table 2. The phase-averaged fluxes

Telescope	Date ^a (MJD TDB)	Exposure time (ks)	Observation ID	Name ([t]YYMMDD)
<i>XMM-Newton</i> ^b	53994.791448810	46.0	0404340101	060916
	54000.527619667	29.2	0311792001	060922
<i>Chandra</i> ^c	54005.283617719	15.7	6724	c060927
	54009.985545836	20.7	6725	c061002
	54017.265934068	26.2	6726	c061009
	54036.293110632	15.7	8455	c061028
	54133.801451742	20.6	8506	c070113
<i>XMM-Newton</i> ^b	54148.378135941	17.6	0410580601	070217
	54331.412027612	23.7	0505290201	070819
	54511.305592759	29.8	0505290301	080215
	54698.508875675	30.7	0555350101	080820
	55067.333418577	41.4	0604380101	090824
<i>Swift/PC</i> ^d	55823.887347023	3.1	00030806020	
	55829.233491897	4.3	00030806022	
<i>Swift/PC</i> ^d	55831.936336540	16.7	0679380501	110927
	55835.185790895	3.7	00030806023	
	55839.066673333	3.7	00030806024	
	55842.093900977	3.9	00030806025	
	55844.092375078	4.0	00030806026	
<i>Chandra</i> ^c	55849.040224474	8.8	00030806027	
	55857.646333201	19.1	14360	c111023
<i>Swift/PC</i> ^d	55974.223899273	0.6	00030806028-29	
	56001.015943907	2.4	00030806031	

^a Start of observation (post-reduction).

^b In all *XMM-Newton* observations EPN detector was used.

^c In all *Chandra* data ACIS detector was used.

^d In all *Swift* observations we refer to the XRT

Table 1. Summary of the observational data used in the paper

and periods for the 2011 outburst, as derived from the *XMM-Newton* and *Chandra* pointings, were reported by An et al. (2013). A detailed spectral and timing analysis is first reported in this paper where we present an extended, phase coherent long-term timing solution and phase-resolved spectroscopic analysis for both outbursts. The implications, within the magnetar scenario, are also discussed by means of state-of-the-art magnetothermal evolution simulations.

2 OBSERVATIONS AND DATA PROCESSING

For the 2006 outburst analysis we used data from eight *XMM-Newton* and five *Chandra* observations. For the 2011 outburst one *XMM-Newton*, one *Chandra* and nine *Swift* observations were used. A detailed log of all the collected data can be found in Table 1.

The data reduction were performed following standard procedures and consisted of initial raw data calibration; filtering, including from solar flares and soft photons falres; correcting the photon’s arrival times to the barycenter of the Solar system; source and background extraction; pileup checks; and spectral data rebining and oversampling (see Section 4 for details). The reduction procedures were performed using the official Science Analysis System (SAS) package (version 12.0.1 release: XMM-SAS_20110223_1801-11.0.0) for the *XMM-Newton* data, and the Chandra Interactive Analysis of Observations (CIAO) system (version 4.4) for the *Chandra* data. The *Swift* data were processed and filtered with standard procedures and quality cuts¹ using FTOOLS

¹ See <http://swift.gsfc.nasa.gov/docs/swift/analysis/> for more details.

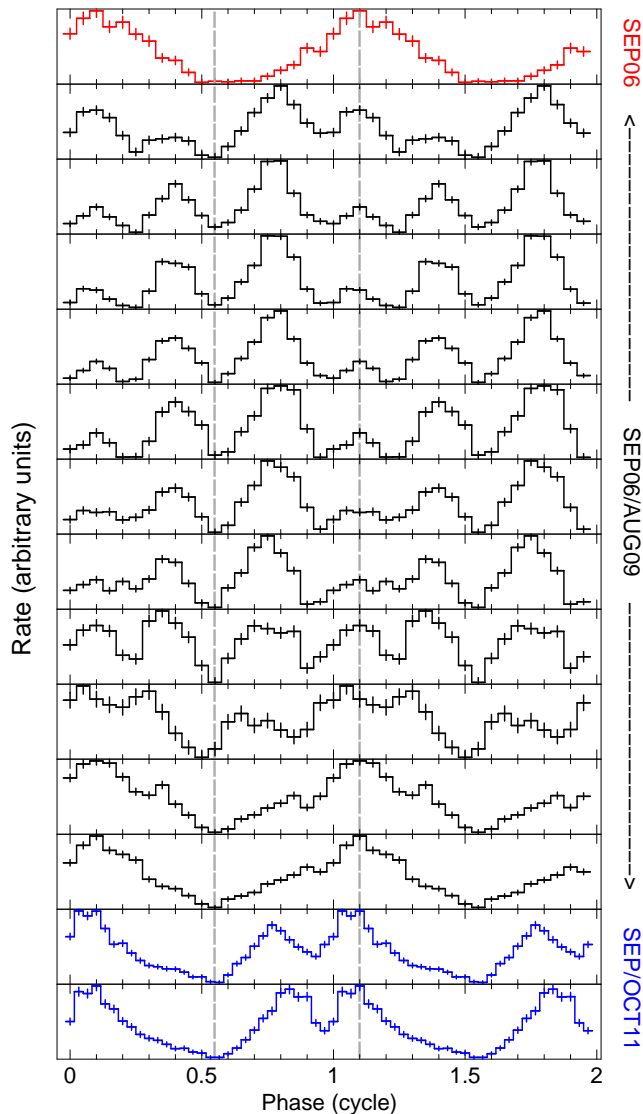


Figure 2. Pulse shape evolution over time. *XMM-Newton* 2006 pre-outburst observation (red line), *XMM-Newton* and *Chandra* data during 2006 outburst by using our phase-coherent timing solution (black lines), and *XMM-Newton* and *Chandra* data during 2011 outburst (blue lines). Both the 2006 pre-outburst and 2011 outburst folded light curves have been shifted in phase in order to align their minima with those of the 2006 outburst. For better visualization the data has been normalized to the average intensity, the pulse fraction values and its evolution are shown in Fig. 5.

tasks in the HEASOFT software package (v.6.12) and the calibration files in the 2012-02-06 CALDB release.

For the spectral analysis we used XSPEC (version 12.7.1) and for the timing, XRONOS (version 5.22) and pipelines developed in-house for the phase-fitting procedures.

3 TIMING

3.1 2006 – 2009 Outburst

For the timing analysis of the 2006 – 2009 outburst, we used all the data (see Table 1) between 060922 and 090824.

With the only exception of 090824, all the pulse profiles used in the timing analysis present a three-peaked structure, the rela-

tive amplitudes and phases of the peaks were such that it was not straightforward to unambiguously follow the signal phase evolution throughout the outburst decay. To pinpoint the correct signal phase evolution we combined information from the peaks relative (phase) positions and spectral data. For instance, the first peak (see reference on Fig. 1) tends to be wider at higher energies (> 3 keV) while the second one is significantly weaker at low (< 2 keV) energies (See for example Fig. 1; see also Muno et al. 2007).

Based on the above findings we were able to track the peak correspondence for the whole time span from September 2006 to August 2009 (see Fig. 2). We note that during the latter observation the pulse shape had almost returned to the quiescence single-peak profile, while at the beginning of the 2011 outburst the pulses showed again a multiple-peak structure compatible with that of the first observations of the 2006 outburst, though with a rather larger pulsed fraction (see below).

To obtain a phase-coherent timing solution, we started by folding the data into 20 bins per cycle. We considered only events in the 0.5 – 4.0 keV energy interval, since in some observations the shape of the pulse slightly changes at higher energies (see e.g. Fig. 1), which could affect the phase-fitting procedure. We started by dividing the first observation in four segments folded at the period and period derivative reported by Woods et al. 2011 (quadratic fit). Next, we performed the phase-fit procedure obtaining a new solution and repeated the procedure iteratively using the new solution and including the subsequent observation. For details on the phase-fitting procedure see Dall’Osso et al. (2003).

Up to August 2007 (Obs. 070819) a period (P) and period derivative (\dot{P}) components were enough to obtain a phase-coherent timing solution (see Fig. 3, Left panel). After that point a \ddot{P} component becomes necessary (F test at $\sim 4\sigma$ (99.992%) confidence level (c.l.), see Fig. 3 Right panel).

It can be seen in Fig. 3, left panel, that at this epoch the phase connection is maintained marginally at 3σ , (at 5σ the phase coherency is lost and there is a two-cycles ambiguity). While the whole phase-fitting process was performed at a 3σ c.l., in this marginal case we performed an additional test: we separately assumed each of the possible (at 5σ c.l.) cycles as correct and continued parallelly the phase-fitting iteration with the next observation(s), obtaining two different phase evolution tracks. Then, we look if any of the phase track works well without the addition of any further, higher order components, other than those already present in the solution (constant, linear, quadratic and cubic terms). We found that actually only one track yielded a feasible solution, and it coincided with the one found initially at the 3σ c.l., see Fig. 3, right panel.

For all the observations in the 2006 September 22 - 2009 August 24 time interval (Fig. 4) the resulting phase-coherent solution based on phase residual versus time fits gave a best-fitting $P=10.61065583(4)$ s, $\dot{P}=9.72(1)\times 10^{-13}$ s/s and $\ddot{P}=-1.05(5)\times 10^{-20}$ s s $^{-2}$ (all with 1σ uncertainty) and MJD 54008.0 as reference epoch, see Table 2. Our solution shows a good consistency with the data, for instance the χ^2/dof for the whole set of data (*XMM-Newton* and *Chandra*) is 8.95/8 (see Fig. 4).

Note that since we focused on a long-term timing solutions, the reported glitch (Israel et al. 2007) near the outburst onset characterized by a short recovery time of ~ 1 week, does not affect our solution. Earlier works have looked into it, see Israel et al. (2007) and Woods et al. (2011); the detailed short-time analysis required to look into it is outside the scope of this paper. We only note that the extrapolation of the above reported phase-coherent solution backwards to the first pre-outburst observation implies a $\Delta\phi$ of ~ 0.06

Summary of CXOU J164710.2-455216 timing solutions for the 2006-2009 outburst decay						
Epoch (MJD)	Period (s)	\dot{P}^a (10^{-12} s/s)	\ddot{P}^b (10^{-20} s s $^{-2}$)	$B \times 10^{14}^c$ (Gauss)	Notes	
Israel et al. 2007	53999.0	10.6106549(2)	0.92(4)	-	1.0	Coherent, Quadratic fit
Woods et al. 2010	54008.0	10.6106563(1)	0.83(2)	-	0.95	Coherent, Quadratic fit
Woods et al. 2010	54008.0	10.6106558(2)	1.3(1)	-10(1)	1.21 ^d	Coherent, Cubic fit
An et al. 2013	53999.1	10.61064(2)	<0.4(6)	-	< 0.7	Non-coherent, linear fit
This work	54008.0	10.61065583(4)	0.972(1)	-1.05(5)	1.04	Coherent, Cubic fit

^a Period time derivative

^b Second period time derivative

^c $P - \dot{P}$ estimated surface dipolar magnetic field at reported epoch, assuming an orthogonally rotating neutron star of radius 10 km and moment of inertia 10^{45} g cm 2 .

^d Instant value at reported epoch. Note that in Woods et al. (2011) only the average value over the time span of their analysis is reported (0.89×10^{14} G).

Table 2. Summary of previous timing solutions

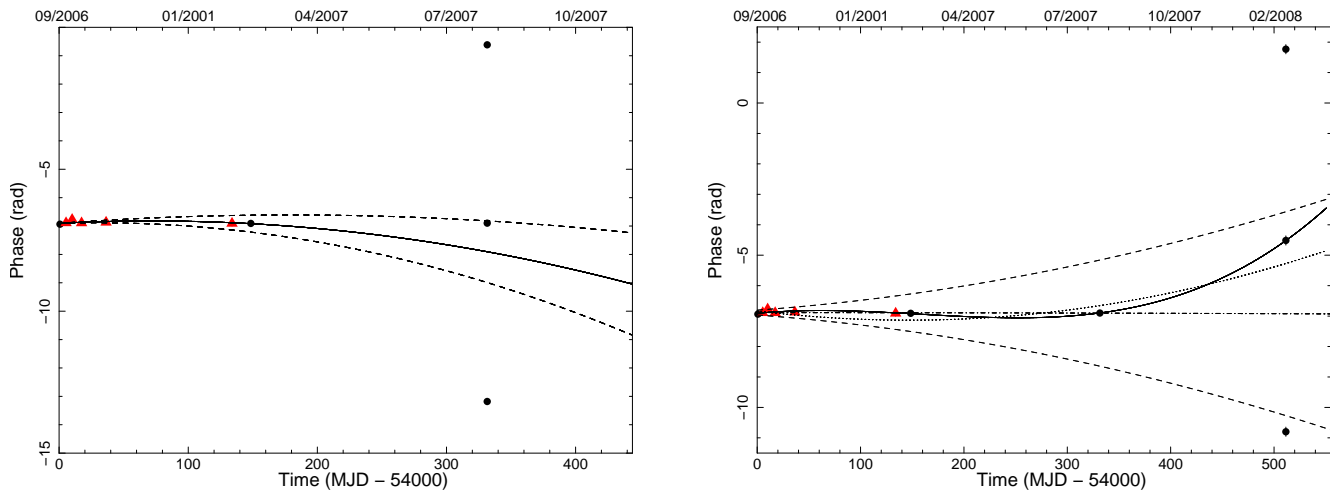


Figure 3. Left panel: phase connected observations up to Feb. 2007 (~ 148 d) using only P and \dot{P} terms. A quadratic fit (solid line) and a 3σ area of its parameters (delimited by dashed lines) are shown. It defines the area where there is a 3σ certainty of phase coherence. For the next observation, Aug. 2007 (~ 331 d), one and only one cycle falls inside the delimited area, thus phase coherence is maintained at a 3σ confidence level and we proceed to correct and extend our timing solution. Right panel: the dashed-dot line represents the timing solution up to Aug. 2007 (~ 331 d) with only P and \dot{P} terms. Correspondingly, the cone delimited by dashed lines represent the area where there is a 3σ certainty of phase coherence for that solution. Solid line: subsequent cubic (P , \dot{P} and \ddot{P}) timing solution. Dotted line: best quadratic fit (black circles are *XMM-Newton* data, red triangles represent *Chandra* observations).

cycles, and a $\Delta\nu/\nu \sim 1.8(6) \times 10^{-5}$, in agreement with an upper limit for $\Delta\nu/\nu < 1.5 \times 10^{-5}$ reported by Woods et al. (2011).

We also studied the evolution of the pulsed fraction, defined as the semi-amplitude of the sinusoid divided by the average count rate. Because of the complexity of the pulse shape, in many cases three sinusoids are needed in order to well reproduce the profiles. We inferred the square root of the quadratic sums of the semi-amplitude of each sinusoid as a rather better estimate of the profile pulsed fraction. The latter quantity is shown in Fig. 5 as a function of time since the first, pre-outburst *XMM-Newton* pointing.

3.2 2011 Outburst

We started by inferring an accurate P measurement for the *XMM-Newton* observation 110927 by means of a phase-fitting algorithm

similarly to the approach adopted for the 2006 outburst data. We found a best period of $P = 10.61066(1)$ s. The relative accuracy was enough to phase-connect further data sets.

The relative phases and amplitudes are such that the signal phase evolution could be followed unambiguously for the *Swift* and *Chandra* observations carried out during the 19 September 2011 - 23 October 2011 time interval (see latest two folded light curves in Fig. 2 for *XMM-Newton* and *Chandra*). Within this interval a term taking into account for the period evolution started to be statistically needed. By adding a quadratic component to the phase history we obtained a best-fitting period of $P = 10.610673(2)$ s and $\dot{P} = 3.5(1.0) \times 10^{-12}$ s s $^{-1}$ (1σ uncertainties are reported; epoch = 55823.0 MJD; $\chi^2/\text{dof} = 11/7$). The subsequent source seasonal visibility window opened in February 2012 during which two further *Swift* pointings were carried out. Unfortunately a rela-

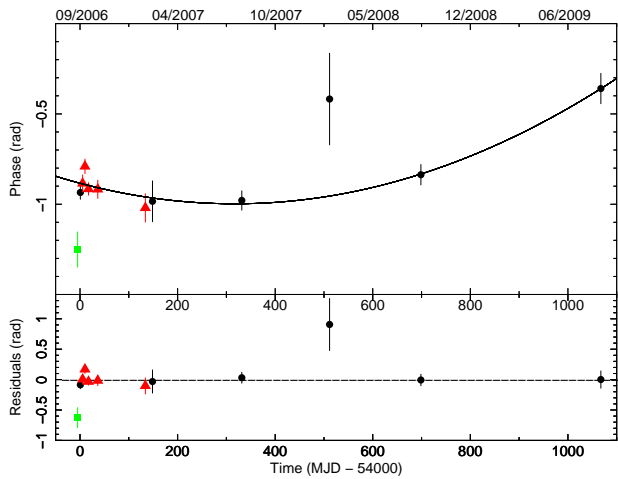


Figure 4. Upper panel: Phases of the *XMM-Newton* (black circles) and *Chandra* (red triangles) observations of CXOU J164710.2–455216 minus a cubic component. The solid line represents the final timing solution. Lower panel: fit residuals. The green square represents the pre-outburst *XMM-Newton* observation (060916).

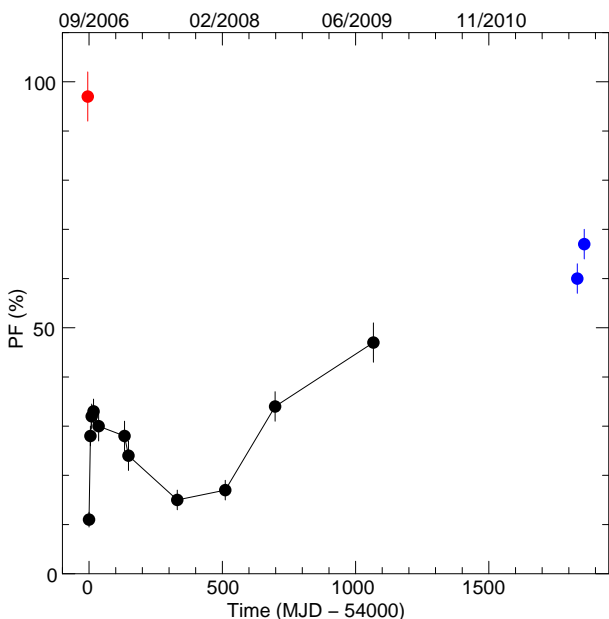


Figure 5. Evolution of the pulsed fraction (see the text for definition) as a function of time (in truncated JD): black filled circles mark the 2006–2009 CXOU J1647–45 outburst, while the pre-outburst and 2011 outburst values are reported in red and blue, respectively.

tively long *XMM-Newton* pointing, scheduled on March 2012, was deleted due to bad space weather (intense solar storm). We therefore used the remaining two low-statistics *Swift* pointings in order to further refine the 2011 timing solution.

Unfortunately, the 2011 timing solution accuracy was not good enough to keep unambiguously the coherence until the 2012 *Swift* pointings, and as a consequence three different solutions become, therefore, possible (starting from low \dot{P} to larger values): (a) $P = 10.6106787(4)$ s and $\dot{P} = 7(1) \times 10^{-13}$ s s $^{-1}$ ($\chi^2/\text{dof} = 19/9$), (b) $P = 10.6106761(4)$ s and $\dot{P} = 2.2(1) \times 10^{-12}$ s s $^{-1}$ ($\chi^2/\text{dof} = 19/9$), and (c) $P = 10.6106723(4)$ s and $\dot{P} = 4.3(1) \times 10^{-12}$ s s $^{-1}$ ($\chi^2/\text{dof} = 15/9$). We note that solution (a)

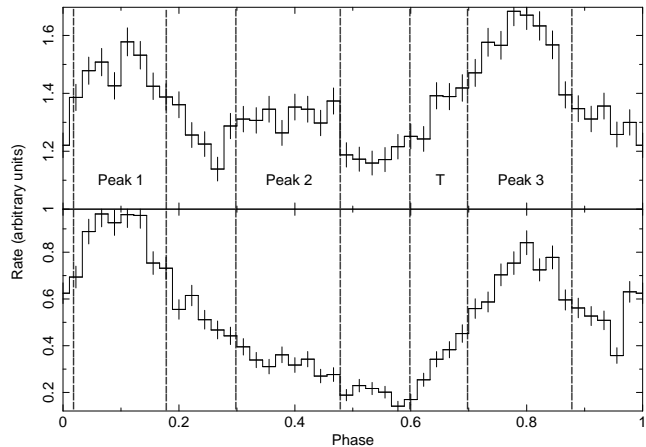


Figure 6. Pulse phase intervals used in the phase-resolved spectroscopy. The phase zero-point is the same as in Fig. 2. The letter “T” denotes the transition region (see text for details). Upper panel: first *XMM-Newton* observation of the 2006–2009 outburst (060916). Lower panel: first *XMM-Newton* observation of the 2011 outburst (110927).

is in agreement, within uncertainties, with the 2006 outburst timing parameters, while solution (c), with a slightly better reduced χ^2 , correspond to a rather high \dot{P} . Moreover, solutions (b) and (c) are within 2σ from the 2011 timing solution, while solution (a) is slightly farther than 3σ .

During the 2011 outburst pulse profiles returns to a multiple-peak configuration, and the pulse fractions are in between those measured for the 2006 pre-outburst observation and for the 2006–2009 outburst (see also Figs. 2 and 5), with the 2011 values being on the extrapolation of the 2008–2009 trend.

4 SPECTRAL ANALYSIS

4.1 2006 – 2009 Outburst

For the spectral analysis we used only the *XMM-Newton* observations in order to rely upon higher statistics data and the same instrument (therefore minimizing the possible intercalibration issues among different detectors). We applied our final timing solution to the data and we performed a pulse phase spectroscopy (PPS) over the whole time interval of validity of the timing solution. Since the pulse profile displays such a complex multipeak structure, where each peak seems to evolve differently (from the point of view of their relative fluxes, see Fig. 2) over time, it was important to study each different component (such as peaks and minima) separately, as a function of time and to find out if there were any spectral peculiarities along the pulse phase.

With this aim in mind we first divided the pulse phase in seven parts: three peaks, three minima and a transition region which shows different spectral characteristics in high (3–12 keV) and low (0.5–2 keV) energies, with respect to those of the peak adjacent to it (peak 3; see the peaks nomenclature and spectral bins used in the PPS in Fig. 6). This pulse-profile segmentation allows us to follow the evolution of the peaks and the minima with the maximum possible signal-to-noise ratio.

To obtain the phase-resolved spectra, first we used

‘phasecalc’² to calculate the phases on each observation events file. Then used ‘tabgtigen’² and ‘evselect’² to obtain the seven event files per observation filtering by phases and subsequently extract their spectra. ‘arfgen’ and ‘rmfgen’ were used to generate the ancillary response files and the redistribution matrix files, respectively. Then we used ‘grppha’³ to rebin the spectra to ensure that each spectral channel had at least 30 counts and to oversample the instrumental energy resolution by a factor of three.

Previous spectral analysis on this source has been performed by Israel et al. 2007; Woods et al. 2011 and An et al. 2013. In all previous works the average spectra was fitted with an absorbed, single blackbody (BB) plus a Power Law (PL). However, Albano et al. (2010) based their analysis on a more physical model taking into account the effect of the magnetosphere twist. Physical and geometrical parameters were recovered from the joint modeling of the pulse profiles and spectra. The resulting best-fits for the light curves, consisting of three NTZang spectra (Nobili, Turolla & Zane 2008) were then used to fit the observed spectra, mimicking the magnetospheric reprocessing of photons from three regions of the NS surface at different temperatures, obtaining good agreement with the data. (See Albano et al. 2010 for details). We tried a similar spectral decomposition, but due to the relatively high number of free parameters in the latter model and the lower statistics of phase-resolved spectra resulted in a reduced χ^2 systematically lower than 1. Therefore, we decided to use the closest possible model to that used by Albano et al. (2010) by assuming a three absorbed BB components: phabs(bbodyrad1 + bbodyrad2 + bbodyrad3) in XSPEC³. One of the BBs had a fixed temperature of 150 eV which is meant to correspond to the “cool” fraction of the NS surface; and the other two BBs to a hotspot and a warm zone around it (or, in principle, any other two-temperature configuration), and were left free to vary between observations. Representing a thermal map of the whole NS surface, their temperatures, were forced to be the same for all the phase intervals, in each epoch (see Albano et al. 2010 for more details on the geometric model). The absorbing column density was fixed to $2.4 \times 10^{22} \text{ cm}^{-2}$, based on the phase average spectral fits. Such a configuration, with an appropriate spin and magnetic axis and line-of-sight angles, may reproduce the three-peaked pulse profile (see Albano et al. 2010).

In several cases the statistics of the minima’s spectra was not good enough to obtain an acceptable spectral fit, being overfitted by our 1(kT-fixed)+2BB model. Since, the problem of low statistics affected most of them, we decided to focus on the pulse-profile peaks. The resulting BB parameters are presented in Figs. 9, 10 and Table 3. In Fig. 11 dynamic spectral profiles of each peak are presented, in the plots the flux density distribution over the 1–10 keV energy range, over the 3 yr of the 2006 outburst-decay campaign.

Our analysis indicates that, indeed, there are spectral differences between them; both on single observations and on their afterburst relaxing evolution over time (see Figs. 7 and 8). For instance, peak 2 (see reference on Fig. 6) is softer than the others, and peak 1 (which correspond to the quiescence peak), is harder. The temperatures of the BB do not vary significantly. Specially the warm component shows a very steady value of $\sim 0.58 \text{ keV}$. The hot component may be more variable, but the errors do not allow us to draw concrete conclusions in this regard. On the other hand, the evolu-

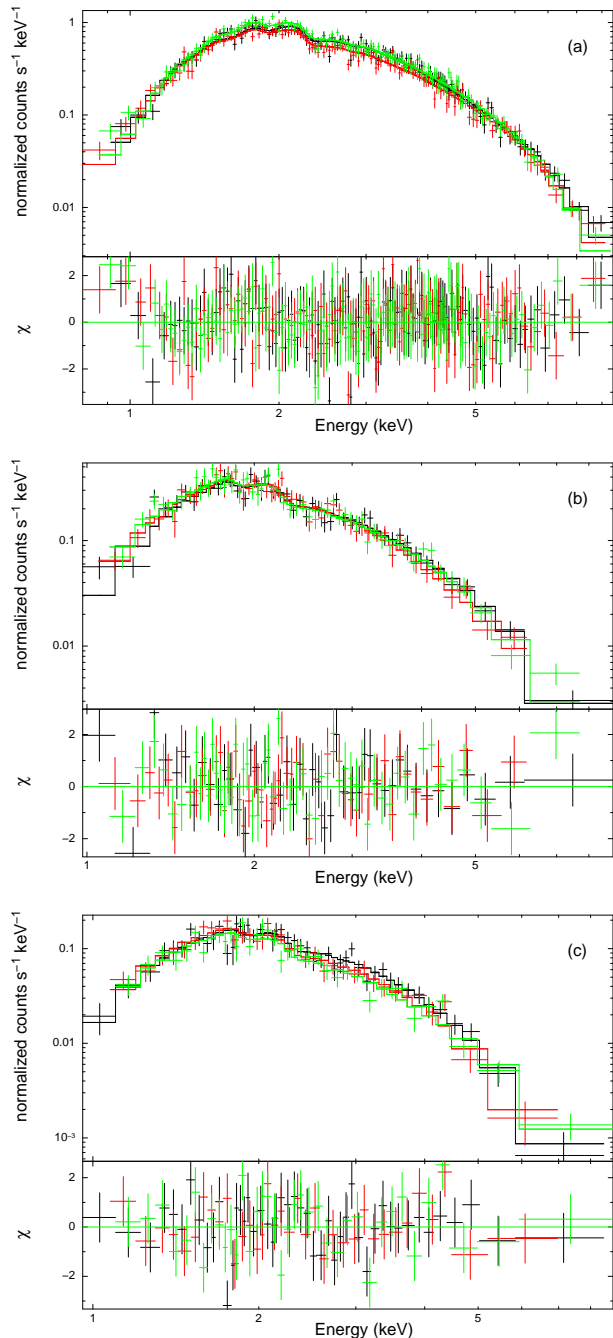


Figure 7. Pulse phase-resolved spectra of the peaks. 060922(a), 070819(b) and 080820(c). Peaks spectral relative evolution at a glance. First peak – black; second peak – red; third peak – green. See Fig. 6 and 2 for peaks reference.

tion of the BB-radius shows a constant and significant shrinking of both components. Indeed, the hot component disappears about 500 d after the outburst onset, see Figs. 9–11 and Table 3.

4.2 2011 Outburst

Using the same phase intervals as for the 2006 outburst data and the 2011 timing solution, we performed a PPS for the first *XMM-Newton* observation of the 2011 outburst. The phase intervals were extracted with the same methods and fitted with the same models

² Part of the Science Analysis System (SAS) package (used version 12.0.1 release: XMMSAS_20110223_1801-11.0.0)

³ Part of HEASoft (used heasoft-6.12)

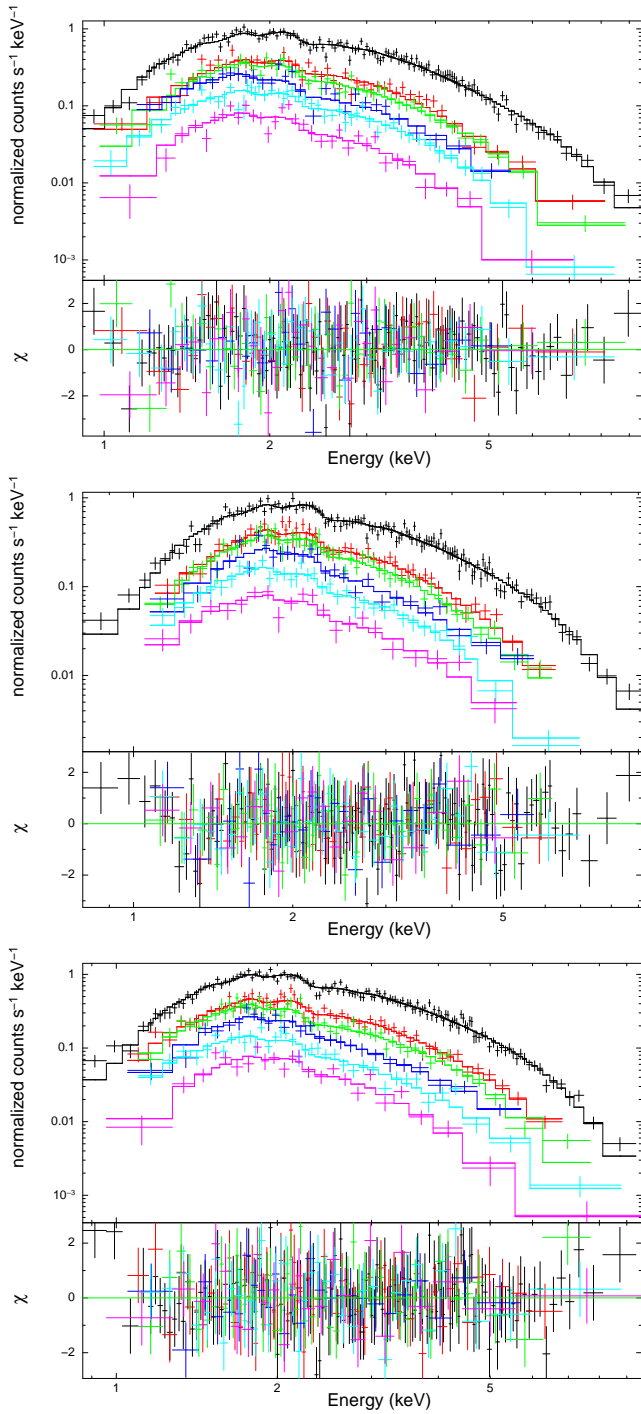


Figure 8. Phase resolved spectral evolution of CXOU J164710.2–455216. The solid lines represent the 1+2BB absorbed model for the peak 1 (upper panel), peak 2 (middle panel) and peak 3 (lower panel), see Fig. 6 and 2 for reference. Black: 060922; red: 070217; green: 070819; blue: 080215; cyan: 080820; magenta: 090824. Residuals are shown in the lower part of each panel.

used for the 2006–2009 data (see Section 4.1); with the new 2011 timing solution and the same peaks identification scheme as for the 2006–2009 data (see Section 3.1). The results are reported in Table 3.

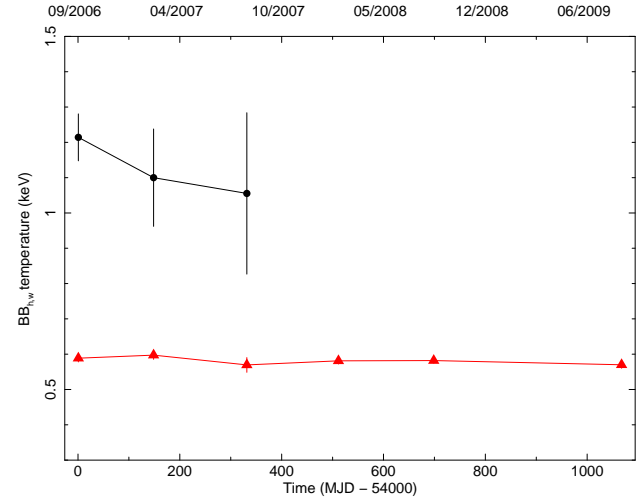


Figure 9. Temperature evolution of the BB used for modeling the peaks spectra. Black circles correspond to the hard component, red triangles to the warm component. The zero point in time represents the onset of the 2006 outburst.

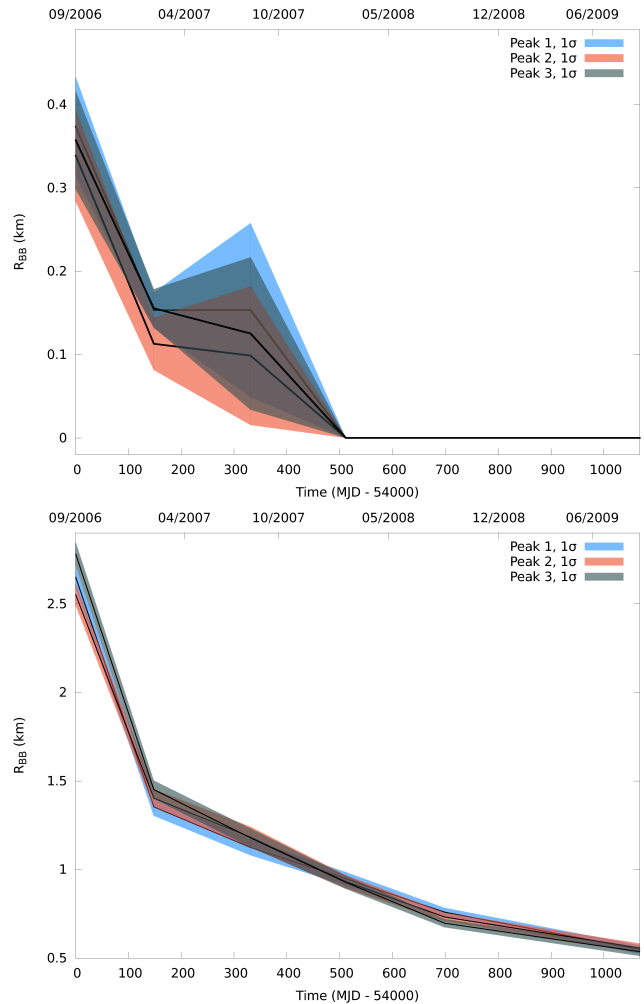


Figure 10. Evolution of the blackbodies radii (R_{BB}) used for modeling the peaks spectra. Upper panel: hard component; lower panel: warm component.

CXOU J164710.2–455216 1+2-blackbody spectral fit					
Peak ^a	Obs. ID	T _w (keV)	R _{BB} ^W (Km)	T _H (keV)	R _{BB} ^H (Km)
First (quiescent) $\chi^2_{red} = 1.1865$	060922	0.59 ± 0.01	2.65 ± 0.06	1.21 ± 0.07	0.37 ± 0.06
	070217	0.60 ± 0.01	1.35 ± 0.05	1.10 ± 0.14	0.15 ± 0.02
	070819	0.57 ± 0.02	1.12 ± 0.05	1.06 ± 0.23	0.15 ± 0.10
	080215	0.58 ± 0.01	0.95 ± 0.04	–	–
	080820	0.58 ± 0.01	0.76 ± 0.03	–	–
	090824	0.57 ± 0.01	0.55 ± 0.03	–	–
	110927	–	–	0.77 ± 0.01	0.23 ± 0.01
Second $\chi^2_{red} = 1.0522$	060922	0.59 ± 0.01	2.55 ± 0.06	1.21 ± 0.07	0.34 ± 0.06
	070217	0.60 ± 0.01	1.40 ± 0.05	1.10 ± 0.14	0.11 ± 0.03
	070819	0.57 ± 0.02	1.18 ± 0.06	1.06 ± 0.23	0.10 ± 0.09
	080215	0.58 ± 0.01	0.93 ± 0.04	–	–
	080820	0.58 ± 0.01	0.73 ± 0.03	–	–
	090824	0.57 ± 0.01	0.56 ± 0.03	–	–
	110927	–	–	0.77 ± 0.01	0.20 ± 0.01
Third $\chi^2_{red} = 1.0516$	060922	0.59 ± 0.01	2.78 ± 0.07	1.21 ± 0.07	0.36 ± 0.06
	070217	0.60 ± 0.01	1.45 ± 0.05	1.10 ± 0.14	0.16 ± 0.03
	070819	0.57 ± 0.02	1.18 ± 0.06	1.06 ± 0.23	0.13 ± 0.09
	080215	0.58 ± 0.01	0.93 ± 0.04	–	–
	080820	0.58 ± 0.01	0.70 ± 0.03	–	–
	090824	0.57 ± 0.01	0.54 ± 0.03	–	–
	110927	–	–	0.77 ± 0.01	0.23 ± 0.01

^a See Figs. 6 and 2 for reference.

Table 3. 1+2BB fit spectral parameters. Obs 110927 corresponds to the successive outburst. See the text for details.

5 DISCUSSION

5.1 Timing

Significant changes in the pulse profile during the outburst decay mean that peaks identification and the way of taking into account their variations in relative phase (among peaks), intensity and shape, is important in order to successfully phase connect the observations. For instance Woods et al. (2011) cite the “extreme change in pulse profile” as the reason why they were not able to phase connect the 070819 observation with their coherent solution. On the other hand, An et al. (2013) cite a large time separation between 070819 and the previous observation as the cause of their phase connection loss. As mentioned before (see Fig. 1) at different energy ranges the peaks behave differently. This fact, coupled with measurements of the relative phase distances between peaks allowed us to identify them. Once we obtained a consistent peak identification, we had no problems to keep the phase coherence, see Fig. 3, left panel. We believe that discrepancies with respect to previous published results may be due to the different assumptions used for the phase-fitting algorithm.

The new spin-down value $\dot{P} \simeq 9.7 \times 10^{-13} \text{ s s}^{-1}$ is similar to that of the two previous P and \dot{P} solutions: $\dot{P} \simeq 9.2 \times 10^{-13} \text{ s}$

s^{-1} derived by Israel et al. (2007) and $\dot{P} \simeq 8.3 \times 10^{-13} \text{ s s}^{-1}$ reported by Woods et al. (2011) but significantly smaller than the one of the cubic solution of Woods et al. 2011 ($\dot{P} \simeq 13 \times 10^{-13} \text{ s s}^{-1}$), who considered a shorter data sample spanning from 2006 September 23 to 2007 February 17. This may be due to a decrease of the spin-down rate throughout the outburst decay.

The P and \dot{P} values inferred imply a surface dipolar field $B \sim 1.0 \times 10^{14} \text{ G}$ using the conventional formula at the equator $B = 3.2 \times 10^{19} (P\dot{P})^{-1/2}$, assuming an orthogonally rotating neutron star of radius 10 km and moment of inertia 10^{45} g cm^2 . This estimate lays in the standard magnetar range and agrees with the magnetar nature of CXOU J164710.2–455216.

5.2 Outburst decay

In previous (phase-averaged) studies, spectra have been analyzed during the outburst decay and fitted with an absorbed PL plus a BB (Woods et al. 2011; An. et al. 2013). In those works the BB evolution during the outburst agrees with that of the general trend of the warm components of the outburst peaks of our PPS. Particularly, an almost constant temperature and a shrinking BB radius during the outburst decay (Figs. 9 and 10). To our knowledge, the only

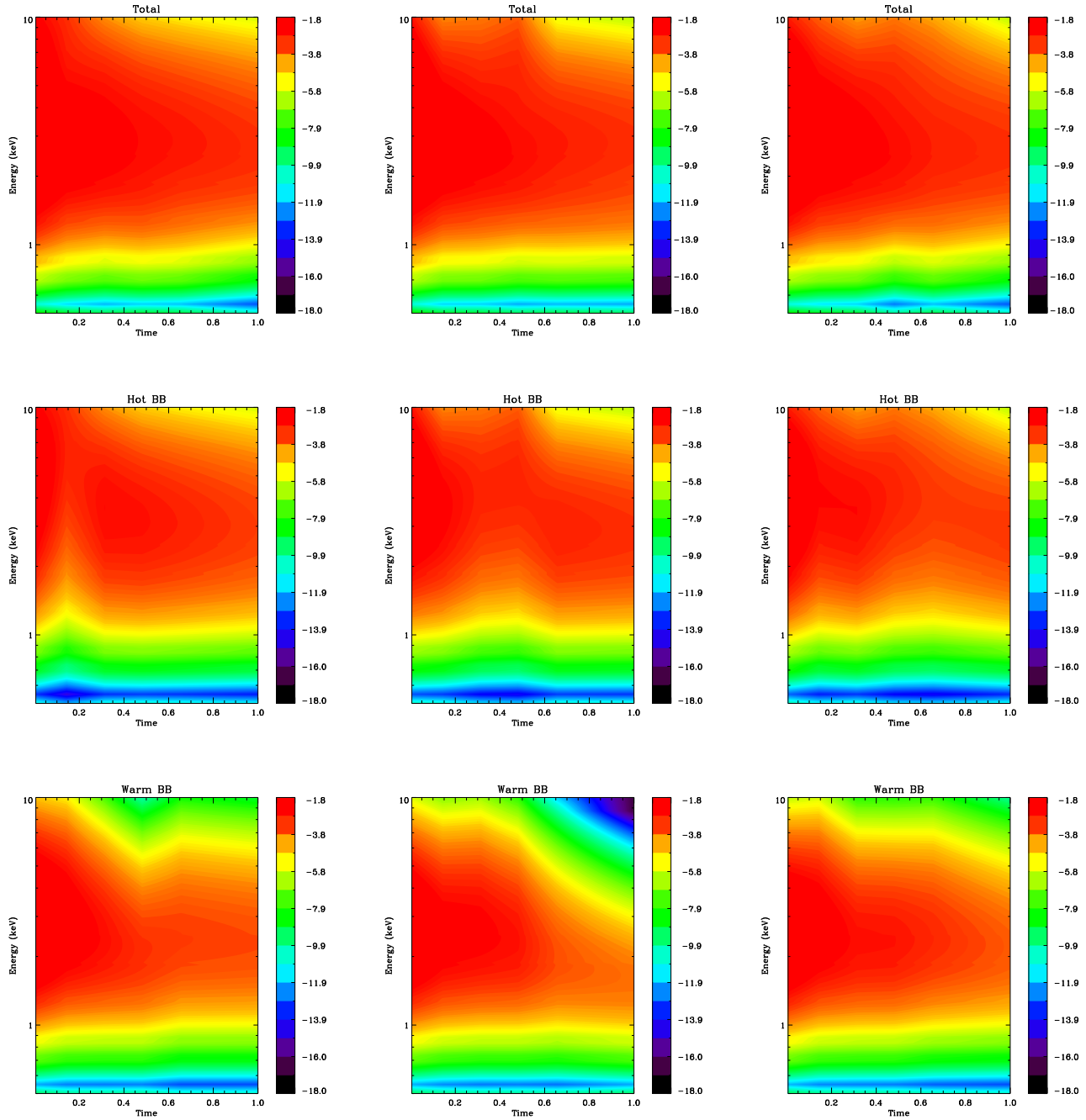


Figure 11. Dynamic spectral profiles. Energy-resolved Flux (colors) evolution over the duration of the 2006 outburst campaign for the three pulse-profile peaks. Each column corresponds to one of the peaks: first (left), second (center) and third (right). The three rows represent in the time/energy plane the contour plots for the total (upper), hot BB (middle) and warm BB (lower) νF_ν fluxes. The color scale is in log units of keV^2 ($\text{photons cm}^{-2} \text{s}^{-1} \text{keV}^{-1}$). The x-axis is time MJD - 54000, normalized to the duration of the 2006 outburst campaign (~ 1067.5 d).

other work that have performed a spectral analysis over long time-scales is the one of Albano et al. (2010), who, in the framework of the twisted magnetospheric model (Thompson et al. 2002), used three modified BB to model the spectra, similar to the approach we based our work on (see text for details). Taking into account that Albano et al. (2010) did not perform a spectral fit, but obtained the physical parameters from synthetic pulse profiles, and, more importantly, that their values correspond to phase-average spectra, it is difficult to make a direct comparison with our results. Nonetheless, the thermal evolution of the BB modeled on Albano et al. (2010) is

very similar to the one we infer: a constant warm component and a slightly decreasing value of the hot component temperature, while still consistent with a constant within the 1σ errors. Likewise, the radius evolution of the hot component in Albano et al. (2010) is as well very similar to the one we infer for the peaks: it significantly decreases throughout the outburst decay, ultimately disappearing in about 700 d. On the other hand, in Albano et al. (2010) the warm component increases in size throughout the outburst, in contrast with what we infer in this work. Yet, the analysis of another magnetar considered by Albano et al. (2010), XTE J1810-197, show the

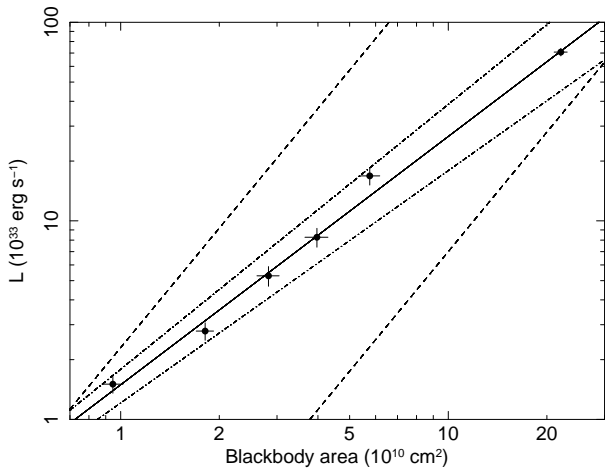


Figure 12. Luminosity versus emitting area of the warm BB component of the third peak (See Fig. 6 and 2 for reference). The dashed lines represent the $L \propto A^2$ of simple untwisting magnetosphere models, see Beloborodov, (2009). The solid line is a PL fit to the data which yields $L \propto A^{1.25}$. The dot-dashed lines represent the 3σ uncertainty of the fit (and correspond to $L \propto A^{1.17}$ and $L \propto A^{1.34}$).

same decay trend we see in the outburst peaks: the hot and warm components keep an almost constant temperature and fade away in size, leaving the star emitting at the quiescence temperature towards the end of the outburst decay (in the case of a third, constant, “cool” BB temperature, see Albano et al. 2010 for details).

Prior to the outburst, the pulse profile of the CXOU J164710.2–455216 was single-peaked. The outburst strongly changes the observed pulse profile, and a three-peaked structure is clearly seen from the onset and during most of the outburst. Nevertheless, as the outburst decays, the pulse profile evolves and towards the end of the 2006 campaign, as the luminosity decreases, and CXOU J164710.2–455216 returns to its quiescence level, the pulse profile “returns” to a single-peaked structure. The remaining peak correspond to the peak 1, and it is plausibly to assume that it correspond to the quiescence single peak.

The radius shrinking decay picture fits into the untwisting magnetosphere (UM) model (Beloborodov, 2009), where current-carrying “j-bundles” with twisted magnetic fields gradually shrink. A simple UM model predicts the relation $L \propto A^2$ between the luminosity and the emitting area (see Beloborodov 2009, Equation 48); in Fig. 12 we compare the emitting area evolution with luminosity decay for the warm component of the third peak with this modeled relationship. The PL fits well the data but our analysis suggests a somehow flatter dependence than expected by the simple model, see Fig. 12.

An important issue is that this interpretation is model-dependent and modeling the data with other spectral components can potentially yield a different picture. Indeed, other non-purely thermal models may also fit well the data, for instance, a BB+PL model and a resonant cyclotron Scattering (RCS) model (Rea et al. 2008) also fit the data acceptably. For instance, the fit for 060922, the best observation in terms of signal-to-noise ratio, has $\chi_{red}^2 = 0.97252$ (130 dof) and $\chi_{red}^2 = 1.0993$ (130 dof), for the BB+PL and the RCS models respectively. While our 1+2BB model has $\chi_{red}^2 = 1.0210$ (129 dof).

On the other hand, independently from the spectral analysis the non-zero, negative second period derivative can also be accounted for within the UM model, as the magnetic field untwists,

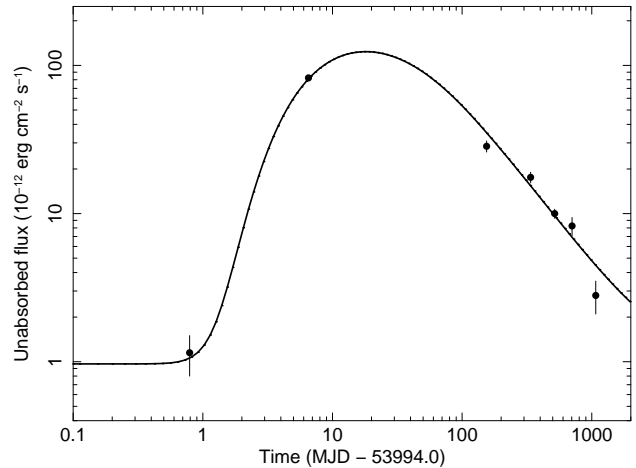


Figure 13. Time evolution of the 0.5-10 keV unabsorbed flux, compared to the predicted light curve of the model discussed in the text.

the spin-down torques diminish, effectively lowering the spin-down rate. However, there may be other explanations to the observed second period derivative, as wind braking, see e.g. Tong et al. (2013).

Furthermore, we also compared the observations of the 2006 outburst with the theoretical model presented in Pons & Rea (2012). The pre-outburst model is taken to be the evolved NS that fits the present observational constraints. Then we assume that the source undergoes a sudden starquake, possibly with internal magnetic re-connection, which we model by the injection of energy ($\approx 10^{25}$ - 10^{26} erg cm^{-3}) in the thin layer between two variable densities. We found a good agreement with the luminosity data when the energy is deposited between $\rho = 2 \times 10^9$ and 2×10^{10} g cm^{-3} , precisely in the transition region between the outer crust and the liquid envelope, which may be a hint that the energy is provided not only by elastic energy stored in the solid crust but also by magnetic re-connection in the liquid layer. The time evolution of the unabsorbed flux in the 0.5-10 keV band for this particular model is shown in Fig. 13 and superimposed to the measured flux values. The total injected energy was of 2×10^{43} erg. We note that the last observation seems to show a smaller flux than the prediction of the theoretical model. Interestingly, the same effect has been observed and discussed for SGR 0418+5729 (SGR 0418), where the sudden decrease of the flux after 300 days is not well understood (Rea et al. 2013). The occurrence of a second outburst soon after this last data point, does not allow to determine if the source had fully recovered its quiescence state or it was still cooling down.

Note that a short-term (~ 10 d) rise in temperature early in the outburst onset, reported by An et al. (2013), which may be expected from crustal cooling models is out of the long-term evolution scope of this paper.

5.3 Magnetorotational Evolution

As previously done for other magnetars (SGR 0418 and Swift J1822.3-1606; see Turolla et al. 2011 and Rea et al. 2012b, 2013) we explore if the magnetothermal evolution of a NS born with standard magnetar conditions can lead to objects with properties compatible with those of CXOU J1647 at the present age. We performed some runs using state-of-the-art magnetothermal evolution codes (see Viganò et al. 2013) assuming a $1.4M_{\odot}$ NS with radius $R = 11.6$ km, a short initial period of 10 ms and initial, purely dipolar field of $B = 1.5 \times 10^{14}$ G. In the resulting scenario, the Hall

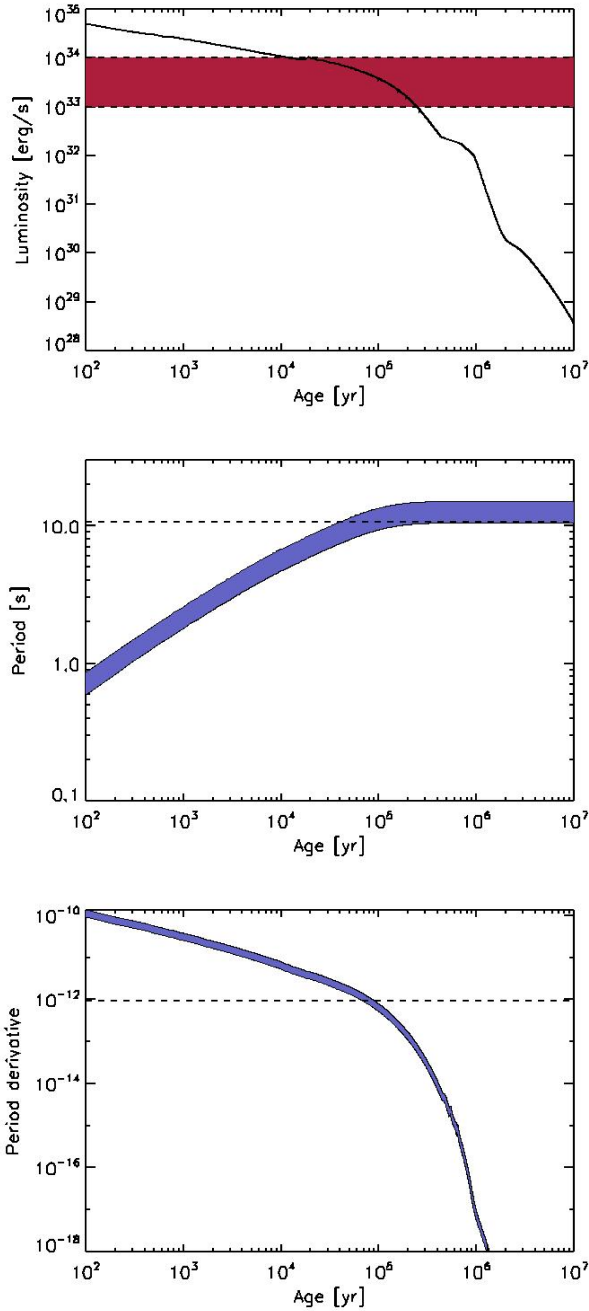


Figure 14. From top to bottom, the evolution of the luminosity, period and period derivative according to the model discussed in the text, compared to the measured values.

term reorganize the internal field, producing a toroidal component of the same strength as the poloidal one on a relatively short time-scale (within a few kyr). We show in Fig. 14 the evolution of the luminosity, period P and period derivative \dot{P} . The latter two quantities are obtained, from the value of the magnetic field at the equator $B(t)$, by numerical integration of the expression (Spitkovsky 2006)

$$P\dot{P} \simeq \frac{4B_e^2 R^6 \pi^2}{Ic^3} (1 + \sin^2 \alpha) \quad (1)$$

where I is the effective moment of inertia of the star, α is the angle between the rotational and the magnetic axis and c is the speed of

light. The shaded blue area in the figure includes the uncertainty in the angle α . Indeed the properties of CXOU J1647 are recovered by this model at an age between 65 and 90 kyr, about half the spin-down age, which suggests that the magnetic field has not experienced dramatic changes over time.

Although the components of the internal initial field $B_{tor}(t = 0)$ can be varied to some extent, this would not change our results unless the toroidal field contains most of the magnetic energy ($> 90\%$), as discussed in Viganò et al. (2013). Moderate values of the initial toroidal field (or higher order poloidal multipoles), are unconstrained and will result in very similar properties at the present age. We can also estimate the current outburst rate of this source following the procedure of Perna & Pons (2011), which gives $\lesssim 10^{-2} \text{ yr}^{-1}$. Therefore, within our model, the occurrence of a second outburst in 2009, three years after the first outburst, must be connected to the first event. Since the second outburst is less powerful, the pulse profile after it closely resembles the pulse profile after the initial (2006) one, and the pulsed fraction does not present a strong change (as the sharp fall after the 2006 outburst onset), but rather seems to follow the rising trend seen during the outburst (see Fig. 5); it may be speculated that there is a connection between them, of the kind main event + sequel, which could reconcile the model with the observations.

Acknowledgments

The authors would like to thank Tolga Guver for his excellent suggestions during the reviewing process that greatly improved the manuscript. DV was supported by the grants AYA 2010-21097-C03-02, ACOMP/2012/135, AYA 2012-39303 and SGR 2009-811. NR was supported by a Vidi NWO grant, Ramon y Cajal Fellowship, AYA 2012-39303 and SGR 2009-811.

References

- Albano A., Turolla R., Israel G. L., Zane S., Nobili L., Stella L., 2010, *ApJ*, 722, 788
- Alpar M. A., Çalışkan Ş., Ertan Ü., 2013, in Zhang C. M., Belloni T., Méndez M., Zhang S. N., eds, *IAU Symposium Vol. 290 of IAU Symposium, fallback Disks, Magnetars and Other Neutron Stars*. pp 93–100
- An H., Kaspi V. M., Archibald R., Cumming A., 2013, *ApJ*, 763, 82
- Baumgartner W. H., Burrows D. N., Cummings J. R., Gehrels N., Gronwall C., Holland S. T., Kennea J. A., Mangano V., Markwardt C. B., Marshall F. E., Racusin J. L., Sbarufatti B., Sonbas E., Ukwatta T. N., 2011, *GRB Coordinates Network*, 12359, 1
- Beloborodov A. M., 2009, *ApJ*, 703, 1044
- Bernardini F., et al. 2009, *A&A*, 498, 195
- Camilo F., Ransom S. M., Halpern J. P., Reynolds J., 2007, *ApJ*, 666, L93
- Camilo F., Ransom S. M., Halpern J. P., Reynolds J., Helfand D. J., Zimmerman N., Sarkissian J., 2006, *Nature*, 442, 892
- Campana S., Israel G. L., 2006, *The Astronomer's Telegram*, 893
- Crowther P. a., Hadfield L. J., Clark J. S., Negueruela I., Vacca W. D., 2006, *MNRAS*, 372, 1407
- Dall'Osso S., Israel G. L., Stella L., Possenti A., Peruzzi E., 2003, *ApJ*, 599, 485
- Duncan R. C., Thompson C., 1992, *ApJ*, 392, L9

- Horvath J. E., 2005, *Modern Physics Letters A*, 20, 2799
- Ibrahim A. I., et al. 2004, *ApJ*, 609, L21
- Israel G. L., Campana S., Dall’Osso S., Munro M. P., Cummings J., Perna R., Stella L., 2007, *ApJ*, 664, 448
- Israel G. L., Esposito P., Rea N., 2011, *The Astronomer’s Telegram*, 3653
- Israel G. L., et al. 2004, *ApJ*, 603, L97
- Israel G. L., et al. 2009, *The Astronomer’s Telegram*, 1909
- Malheiro M., Rueda J. A., Ruffini R., 2012, *PASJ*, 64, 56
- Mereghetti S., 2008, *A&ARv*, 15, 225
- Mereghetti S., 2013, *Brazilian Journal of Physics*
- Munro M. P., et al. 2006, *ApJ*, 636, L41
- Munro M. P., Gaensler B. M., Clark J. S., de Grijs R., Pooley D., Stevens I. R., Zwart S. F. P., 2007, *MNRAS: Letters*, 378, L44
- Negueruela I., Clark J. S., Ritchie B. W., 2010, *AAp*, 516, A78
- Nobili L., Turolla R., Zane S., 2008, *MNRAS*, 386, 1527
- Ouyed R., Leahy D., Niebergal B., 2010, *AAp*, 516, A88
- Paczynski B., 1990, *ApJL*, 365, L9
- Perna R., Pons J. A., 2011, *ApJ*, 727, L51
- Pons J. A., Rea N., 2012, *ApJ*, 750, L6
- Rea N., Esposito P., 2011, *High-Energy Emission from Pulsars and their Systems, Astrophysics and Space Science Proceedings*, p. 247
- Rea N., et al. 2012, *ApJ*, 754, 27
- Rea N., et al. 2013, *ApJ*, 770, 65
- Rea N., Pons J., Torres D. F., Turolla R., 2012, *ApJ*, 748, L12
- Rea N., Zane S., Turolla R., Lyutikov M., Götz D., 2008, *ApJ*, 686, 1245
- Spitkovsky A., 2006, *ApJL*, 648, L51
- Thompson C., Duncan R. C., 1995, *MNRAS*, 275, 255
- Thompson C., Lyutikov M., Kulkarni S. R., 2002, *ApJ*, 574, 332
- Tiengo A., et al. 2013, *Nature*, 500, 312
- Tong H., Xu R. X., Song L. M., Qiao G. J., 2013, *ApJ*, 768, 144
- Turolla R., P. E., 2013, preprint (arXiv:1303.6052)
- Turolla R., Zane S., Pons J. a., Esposito P., Rea N., 2011, *ApJ*, 740, 105
- van Paradijs, J.; Taam, R. E.; van den Heuvel E. P. J., 1995, *A&A*, 299, L41
- Viganò D., Rea N., Pons J. A., Perna R., Aguilera D. N., Miralles J. A., 2013, *MNRAS*, 434, 123
- Woods P. M., et al. 2000, *ApJ*, 535, L55
- Woods P. M., Kaspi V. M., Gavriil F. P., Airhart C., 2011, *ApJ*, 726, 37
- Xu R., 2007, *Advances in Space Research*, 40, 1453